

New data support the existence of the Hercules-Corona Borealis Great Wall

István Horváth¹, Zsolt Bagoly², Jon Hakkila³, and L. Viktor Tóth²

¹ National University of Public Service, Budapest, Hungary,

² Eötvös University, Budapest, Hungary

³ University of Charleston South Carolina at the College of Charleston, Charleston, SC, USA,

Received August, 2014 / Accepted ber, 2015

ABSTRACT

Context. Several large structures, including the Sloan Great Wall, the Huge Large Quasar Group, and a large gamma-ray burst cluster referred to as the Hercules-Corona Borealis Great Wall, appear to exceed the maximum structural size predicted by Universal inflationary models. The existence of very large structures such as these might necessitate cosmological model modifications.

Aims. Gamma-ray bursts are the most luminous sources found in nature. They are associated with the stellar endpoints of massive stars and are found in and near distant galaxies. Since they are viable indicators of the dense part of the Universe containing normal matter, the spatial distribution of gamma-ray bursts can serve as tracers of Universal large-scale structure.

Methods. An increased sample size of gamma-ray bursts with known redshift provides us with the opportunity to validate or invalidate the existence of the Hercules-Corona Borealis Great Wall. Nearest-neighbour tests are used to search the larger sample for evidence of clustering and a bootstrap point-radius method is used to estimate the angular cluster size. The potential influence of angular sampling biasing is studied to determine the viability of the results.

Results. The larger gamma-ray burst database further supports the existence of a statistically significant gamma-ray burst cluster at $1.6 \leq z < 2.1$ with an estimated angular size of 2000-3000 Mpc.

Conclusions. Although small number statistics limit our angular resolution and do not rule out the existence of adjacent and/or line-of-sight smaller structures, these structures must still clump together in order for us to see the large gamma-ray burst cluster detected here. This cluster provides support for the existence of very large-scale universal heterogeneities.

Key words. Gamma-ray burst: general – Methods: data analysis – Methods: statistical – Cosmology: large-scale structure of Universe – Cosmology: observations – Cosmology: distance scale

Use \titlerunning to supply a shorter title and/or \authorrunning to supply a shorter list of author.

1. Introduction

The high luminosities of gamma-ray bursts (GRBs) make them ideal candidates for probing large-scale Universal structure. Gamma-ray bursts signify the presence of stellar endpoints and thus trace the location of matter in the universe. This is true whether they are long bursts (presumably originating from hypernovae), short bursts (presumably originating from compact objects), or intermediate bursts (with unknown origins that are still likely related to stellar endpoints). Assuming that the Universe is homogeneous and isotropic on a large scale implies that the large-scale distribution of GRBs should similarly be homogeneous and isotropic. The angular isotropy of GRBs has been well-studied over the past few decades (Briggs et al. 1996; Balázs et al. 1998, 1999; Mészáros et al. 2000; Magliocchetti et al. 2003; Vavrek et al. 2008). For the most part, GRBs are distributed uniformly, although some subsamples (generally believed to be those with lower luminosities and therefore thought to be cosmologically local) appear to deviate from isotropy (Balázs et al. 1998; Cline et al. 1999; Mészáros et al. 2000; Litvin et al. 2001; Magliocchetti et al. 2003; Vavrek et al. 2008). We have recently identified a surprisingly large anisotropy in the overall GRB angular distribution, suggestive of clustering, at redshift two in the constellations of Hercules and Corona Borealis. The underlying distribution of matter suggested by this cluster is large enough to question standard assumptions about the largest scale of Universal structures.

We revisit the angular and radial distributions of GRBs with known redshifts in an attempt to reexamine our previous claims suggesting the existence of this structure. As of November 2013, the redshifts of 361 GRBs have been determined¹; this represents an increase in sample size of 28% over that used in our previous analysis (283 bursts observed up until July 2012). The number of GRBs in the $z = 2$ redshift range, where the cluster resides, has increased from 31 bursts to 44 bursts, a 42% sample size increase that is large enough to warrant an updated analysis. We apply k^{th} nearest neighbour analysis and the bootstrap point radius method to this database composed largely of bursts detected by NASA's Swift experiment.

2. Nearest-neighbour statistics: the largest anisotropy is at $z = 2$

The larger GRB database allows us to re-examine the significance of our prior results. We employ the same statistical tests so as to retain consistency in our methodology and not introduce any potential analysis biases.

The GRB sample is subdivided by redshift z in a manner similar to our previous work (Horváth et al. 2014) so that we can base our angular studies on well-defined distance groupings. The GRB redshift uncertainties are small (many GRB redshifts are quoted to three or four significant figures), so it is possible in theory to create a large number of radial groups or bins and thus maintain a small z -dispersion in the sample. The drawback to this approach is that the 361 burst sample is

¹ <http://lyra.berkeley.edu/grbox/grbox.php> or <http://www.astro.caltech.edu/grbox/grbox.php>

still small, and angular resolution is limited based on the number of bursts in each radial group. We have subdivided the total sample into eight separate cases, containing the following numbers of radial groups: two, three, four, five, six, seven, eight, and nine. These choices allow us to examine bulk anisotropies in the GRB distribution over various distance ranges. However, binning the data limits the angular resolution we can realistically obtain within each radial bin: we are capable of finding large anisotropies. These cases are not independent of one another; each contains the same GRB sample binned differently. A choice of one radial group corresponds to the bulk angular distribution of GRBs in the plane of the sky; we do not analyse group one here, since it does not make use of the carefully measured redshifts we employed. In contrast, the choice of nine radial groups provides us with radial bins with the smallest number of bursts per bin (≈ 40) for which we can make reasonable, quantifiable estimates on bulk anisotropies. When choosing between 2 and 9 radial divisions, we keep the numbers of bursts in each radial group identical. The result of this approach is that we exclude GRBs with the smallest redshifts in some cases. For example, in the four group case the closest GRB (with the smallest redshift) was excluded, therefore, each of the four groups contains 90 GRBs ($361=4\times 90+1$).

We examine the angular burst distributions of each radial group by independently applying the k th nearest-neighbour statistics to the bursts in each group. As an example of our procedure, we consider the four group case again. For each radial group, we calculate the angular separations between all 90 GRBs. All neighbours of each GRB are identified and ranked as the nearest, second nearest, etc. The 90 nearest neighbour separations are collected into a first distribution, the 90 second-nearest neighbour separations are collected into a second distribution, and the process is repeated with each set of neighbours until the orthogonal set is completed with the 89th distribution being composed of the 89th nearest neighbour (farthest) separations. For each group in the four group case, these 89 nearest-neighbour distributions can be compared across the groups using a Kolmogorov-Smirnoff test. As this has been accomplished for the four group case, the same approach can be applied to the available nearest-neighbour distributions for all eight radial groupings (the two group case through the nine group case).

Each of the eight radial groupings indicates that significant anisotropies are present in one specific radial region, as defined by redshift. In other words, most of the k th nearest-neighbour distributions are not significantly different, except those that are close to one specific redshift. The bin containing the largest cluster of GRBs always comes from the redshift range $1.6 \leq z < 2.1$, as found in our previous work (Horváth et al. 2013, 2014). Figure 1 shows an example of when the sample is divided into four radial groups. In this case, each group contains 90 GRBs in the redshift ranges $2.68 \leq z < 9.4$ (group 1), $1.61 \leq z < 2.68$ (group 2), $0.85 \leq z < 1.61$ (group 3), and $0 \leq z < 0.85$ (group 4). For this example, Table 1 shows the probability that the two distributions are different. Boldface type indicates that the significance of the 31st nearest-neighbour distributions of two groups are different by more than 3σ . There are no significant differences within group 1, group 3, and group 4 distributions, but the 31st nearest-neighbour distributions in group 2 are significantly

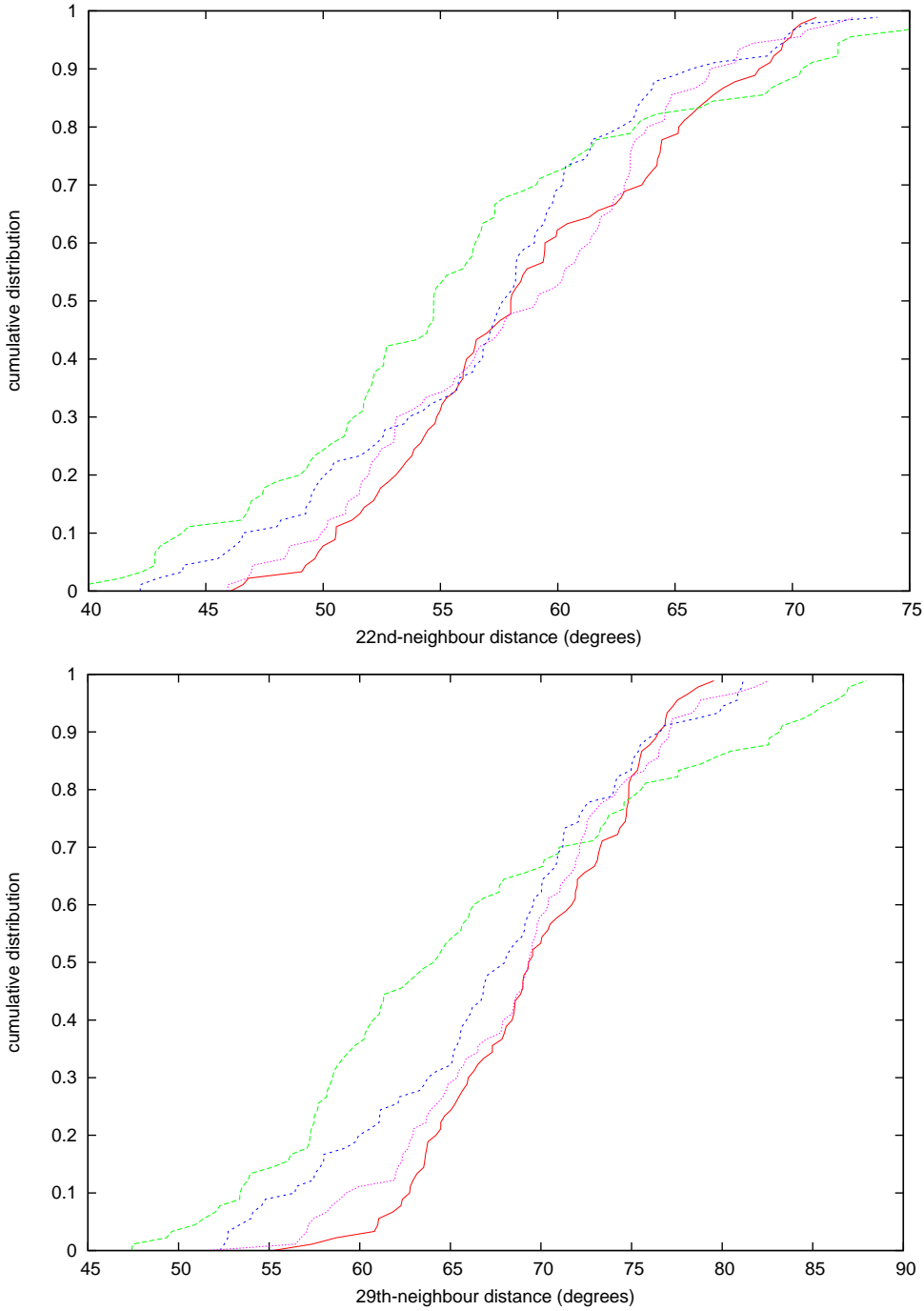


Fig. 1. The 22nd (top) and 29th (bottom) neighbour distribution for the four group case (each group contains 90 GRBs), red, green, blue, and pink identifies radial groups 1, 2, 3, and 4.

different from the other distribution. The 31st nearest-neighbour distribution is just an example demonstrating a group 2 anisotropy; the same is also true for the 22nd, 23rd, ... 55th nearest-neighbour distributions. The GRBs clustering on small angular scales would show differences when describing close neighbour pairs, while GRBs found on opposite sides of the celestial sphere would exhibit differences when describing distant neighbour pairs. The GRBs in the $1.61 \leq z < 2.68$ redshift range have a preference for neighbours with moderately close angular separations, suggesting a large angular cluster.

Table 1. Results of the 31st nearest-neighbour distributions comparing the GRB groups (in the four group case). Comparing the distributions of two groups for the 31st nearest-neighbour, the numbers in this table are the significance of the null hypothesis that the two distributions are different. Boldface type indicates that there are significant (more than 3σ) differences between the two groups.

	z_{min}	gr2	gr3	gr4
gr1	2.68	0.9999999	0.942	0.672
gr2	1.61		0.99904	0.9999988
gr3	0.85			0.960

3. Bootstrap point-radius method: the anisotropy represents a large GRB cluster

As demonstrated in the previous section, nearest-neighbour tests identify pairing consistent with a large, loose GRB cluster in the redshift range $1.6 < z \leq 2.1$. The significance of this cluster can also be measured using other statistical tests designed to identify clustering. Among these is the bootstrap point-radius method described in Sect. 5 of Horváth et al. (2014). The updated data set to which we apply this test contains 44 GRB in the redshift interval $1.6 < z \leq 2.1$.

Our use of the bootstrap point-radius method assumes that the sky exposure is independent of z . To carry out our analysis, we choose 44 GRBs from the observed data set and compare the sky distribution of this subsample with the sky distribution of 44 GRBs with $1.6 < z \leq 2.1$.

To study the selected bursts in two dimensions, we select random locations on the celestial sphere and find how many of the 44 points lie within a circle of predefined angular radius, for example, within 20° . We build statistics for this test by repeating the process a large number of times (i.e., 10000). From the 10000 Monte Carlo runs, we select the largest number of bursts found within the angular circle.

This analysis can be performed with the clustered 44 GRB positions as well as with 44 randomly chosen GRB locations from the observed data. There are some angular radii for which the maximum with the 44 GRBs with $1.6 < z \leq 2.1$ is significant. We repeat the process with 44 different randomly chosen burst positions, and we repeated the experiment 17500 times to understand the statistical variations of this subsample. We also perform the same measurement using angular circles of different radii. The frequencies obtained are shown in Fig. 2.

Figure 2 demonstrates that the 9-18 % of the sky identified for $1.6 < z \leq 2.1$ contains significantly more GRBs than similar circles at other GRB redshifts. When the area is chosen to be $0.0375 \times 4\pi$ (corresponding to an angular radius of $\theta_{max} = 22.3^\circ$), 13 out of the 44 GRBs lie inside the circle. When the area is chosen to be $0.0875 \times 4\pi$ ($\theta_{max} = 34.4^\circ$), 18 of 44 GRBs lie inside the circle. When the area is chosen to be $0.1875 \times 4\pi$ ($\theta_{max} = 51.3^\circ$), 25 GRBs out of the 44 lie inside the circle. In this last case, only two out of the 17500 bootstrap cases had 25 or more GRBs inside the circle. This result is, therefore, a statistically significant ($p=0.0001143$) deviation, and the binomial probability for this being random is $p_b = 2 \times 10^{-8}$.

The 42% increase in sample size should have led to a noticeable decrease in significance if the sample represented random sampling. However, in the radii between roughly 4° and 90° , 49

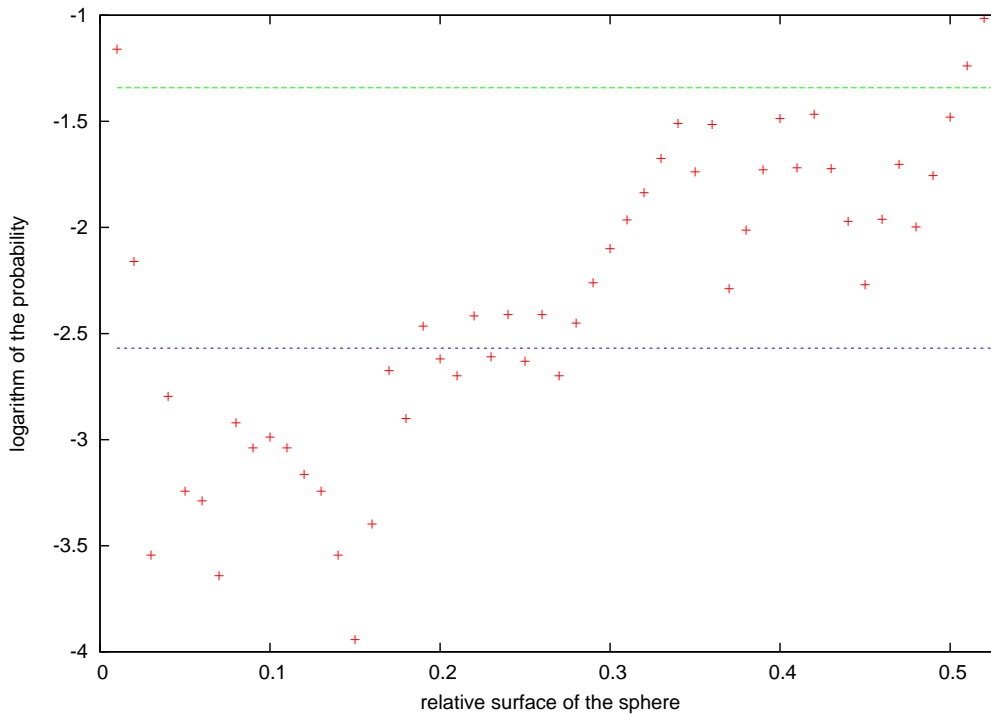


Fig. 2. Results of the Monte-Carlo bootstrap point-radius method. The horizontal coordinate is the area of the circle in the sky relative to the whole sky (4π). The vertical coordinate is the logarithm of the frequency found from the 17500 runs. Green (blue) line shows the 2σ (3σ) deviations.

angular circles contain enough GRBs to exceed the 2σ level, compared to 28 found in our previous analysis (Horváth et al. 2014). Additionally, there are 16 angular circles containing enough GRBs to exceed the 3σ level (compared to only two in our previously published result), therefore, the evidence has strengthened that these bursts are mapping out some large-scale universal structure.

4. Sky exposure: Sampling biases do not appear to be responsible for the anisotropy

Observing biases can introduce measurable angular anisotropies in a sample. However, prior results suggest that these biases are unlikely to be responsible for the observed cluster at $z \approx 2$. The largest potential causes of angular biasing are:

- Sky exposure. This is a well-known bias describing favoured detection of GRBs in some angular directions over others. Sky exposure is a function of instrumental response rather than a true source distributional preference; some causes of anisotropic sky exposure include spacecraft pointing and a preferred orbital plane, the avoidance of certain pointing directions such as the Sun or occultation by the Earth.
- Anisotropic measurement of GRB redshifts. GRB redshift measurements are made in the visual/infrared by ground-based telescopes, and are thus affected by observatory latitudes, seasonal weather, and Galactic extinction.

Each GRB instrument samples the sky differently, making the summed sky exposure difficult to identify for our heterogeneous GRB sample, which has been observed by many instruments since the late 1990s. However, since more than 3/4 of our sample was detected by Swift, the Swift sky exposure dominates the sampling. Thus, we assume to first order that Swift's sky exposure is a reasonable approximation of the sky exposure of the entire burst sample. Because of its orbital characteristics, Swift (Baumgartner et al. 2013) has sampled ecliptic polar regions at slightly higher rates than ecliptic equatorial regions. Our simple model assumes that ecliptic polar regions ($|\beta| \geq 45^\circ$, where β is the ecliptic latitude) are sampled 1.83 times more frequently than the ecliptic equatorial region.

The location of ground-based optical and infrared telescopes measuring GRB redshifts can also lead to anisotropic observations. However, since a large number of ground-based telescopes at a variety of latitudes and longitudes have been used in GRB follow-up observations, there does not appear to be an Earth-based bias that would favour GRB afterglow measurements in some sky locations over others. Thus, our sampling model does not include a term accounting for telescope location.

Extinction due to dust from the Milky Way disk does not affect the detection of GRBs, but it does affect redshift measurements in an angularly-dependent way. Extinction removes light from extragalactic sources, making it harder to measure spectral characteristics from which redshifts can be obtained. Although the Galactic dust is strongly concentrated towards the Galactic equator, it is also very clumpy. This clumpiness makes the effect of extinction on measuring GRB redshifts very difficult to model; the details of the process depends on many variables, such as the Galactic latitude and longitude of the burst, the intrinsic luminosity and decay rate of the afterglow, the light-gathering ability of the telescope and the instrumental response of the spectrograph used, the redshift of the burst, and the observing conditions at the time of detection.

We check to see whether or not the GRB sample favours low-extinction regions by examining the distribution of visual extinctions in the directions of these 361 bursts. Extinctions are obtained from the high angular resolution DIRBE catalogue of Schlafly & Finkbeiner 2011 found online at <http://irsa.ipac.caltech.edu/applications/DUST/>. The results, shown in Fig. 3, are that the sample can be modelled by a lognormal distribution centred at $A_v = 0.13$ mag with standard deviations $\sigma^+ = 0.22$ and $\sigma^- = 0.08$. Fully 91% of the bursts in the sample have visual extinctions of $A_v \leq 0.5$ mag, indicating that a characteristic of a GRB with a measured redshift is that it is not obscured by Galactic extinction.

It is not possible to tell if, in trying to measure GRB redshifts from afterglows, observers have avoided pointing their optical telescopes in the direction of GRBs that lie too close to the Galactic equator. This kind of a bias is possible given the potential low return on afterglow detection (especially for small- and medium-sized telescopes), but this bias cannot be modelled with the limited information provided by optical observers. Since the development of a model describing extinction and extinction-related biases on redshift measurement is very difficult, to estimate the effects of ex-

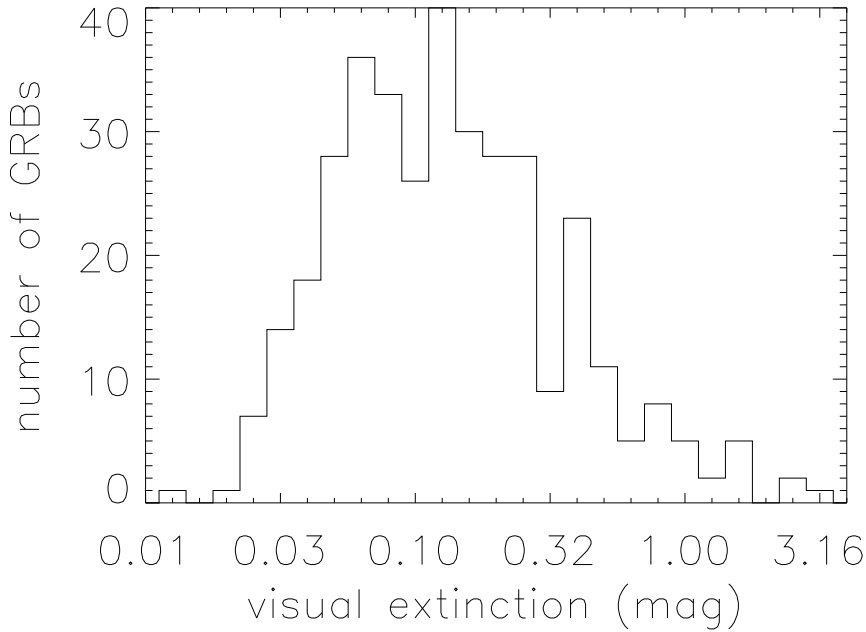


Fig. 3. Galactic visual extinctions in the directions of the 361 GRBs in this sample. The measurement of GRB redshifts strongly favours small amounts of interstellar extinction.

inction on the sample we use all GRBs with measured redshifts found within 20° of the Galactic equator relative to all GRBs with measured redshifts. We find that only 3.1% of the GRB sample has had redshift measurements made within 20° of the Galactic equator.

The Galactic equatorial region is the poorest-sampled region. The ecliptic polar regions ($b \geq 20^\circ$ and $|\beta| \geq 45^\circ$) are the best-sampled regions and the ecliptic equatorial regions ($b \geq 20^\circ$ and $|\beta| < 45^\circ$) are well-sampled regions. Correcting the observations for this biasing, the expected numbers of GRBs in each group are 7.50 (best, north), 7.50 (best, south), 11.2 (good, north), 11.2 (good, south), and 5.54 (poor), whereas the actual counts are 13 (best, north), 2 (best, south), 12 (good, north), 8 (good, south), and 7 (poor). This results in a χ^2 probability of $p = 0.051$ that this is due to chance.

Although this probability is higher than that quoted previously ($p = 0.025$), the cluster density has increased relative to the rest of the $z \approx 2$ sky since the last analysis. Many of the new bursts have been detected just outside the edge of the best-sampled region, in the northern well-sampled region. Unfortunately, our low-resolution angular bias correction treats all GRBs in the well-sampled region as if they are not part of the cluster. If we naively assume that the cluster comprises 17 observed bursts (13 in 50% of the northern best-sampled region and 4 in 10% of the northern well-sampled region) and recalculate the probability that this clustering is random, the probability changes to $p = 1.6 \times 10^{-4}$ that exposure is responsible for the clustering. This calculation also suggests that the cluster properties might be affected slightly by exposure: the few

bursts seen in regions with less exposure could represent a larger number of undetected bursts. The cluster might be shifted several degrees west of where we have previously identified it.

5. Summary and conclusion

The evidence for a possible large-scale Universal structure (Horváth et al. 2014) at a redshift of $z \approx 2$ has strengthened, using a larger database of GRBs with known redshift. The new sample contains 28% more bursts than the previous sample, and 42% more bursts in the $1.6 \leq z < 2.1$ redshift range. Because the cluster has become more populated relative to the rest of the angular distribution at the same redshift, our angular tests have returned more significant results. Nearest-neighbour tests indicate that GRBs in this redshift range favour each others' presence through moderate angular separations. The two-dimensional bootstrap point-radius method reaches the 3σ level for a number of different angular radii, indicating a large GRB cluster. Although sampling biases are present and are significant, these coupled with small number statistics, do not seem to be responsible for the observed clustering of GRBs at this redshift.

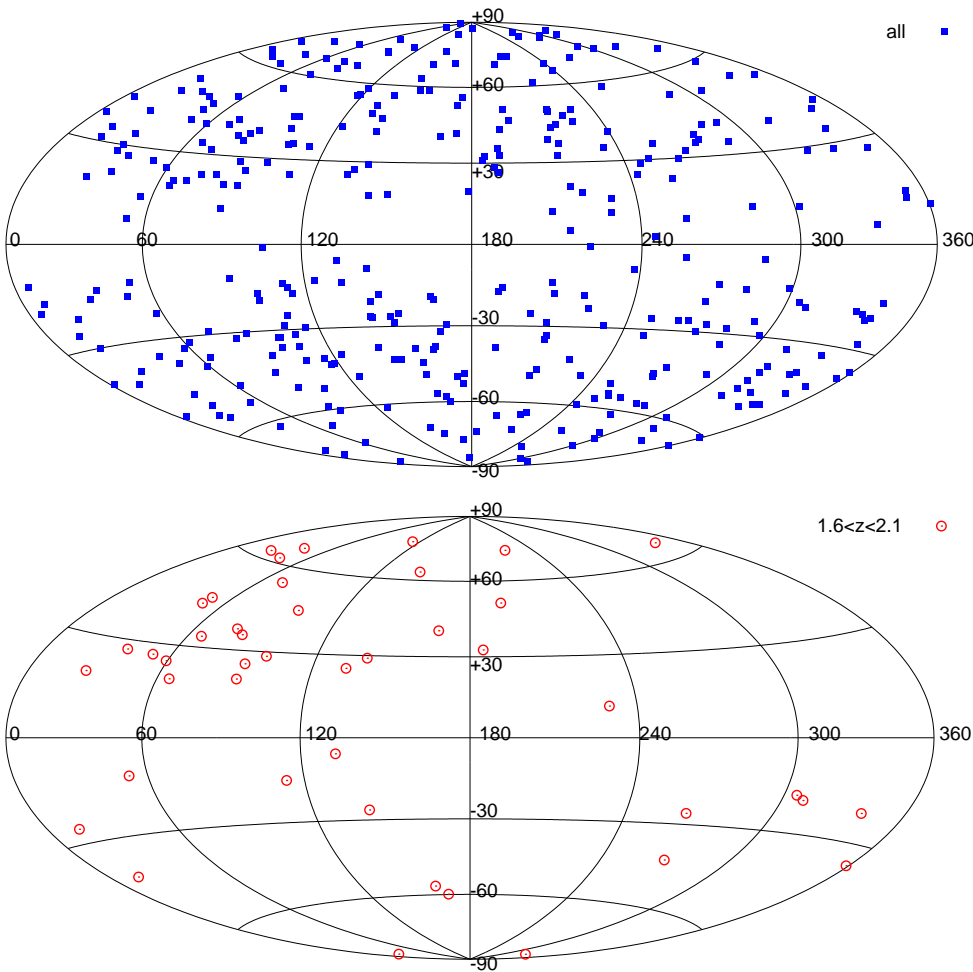


Fig. 4. *Top:* distribution of GRBs with measured redshift (blue). Although the distribution of all GRBs is fairly isotropic, extinction causes this sample to miss GRBs near the Galactic plane. *Bottom:* anisotropic distribution of GRBs near redshift $z = 2$ (red).

GRBs are the most luminous known form of energy release available to normal matter. As such, they are tracers for the presence of normal matter that can be detected at distances where the matter is otherwise too faint to be observed. The GRB cluster at $z \approx 2$ appears to identify the presence of a larger angular structure that covers almost one-eighth of the sky. This encompasses half of the constellations of Bootes, Draco, and Lyra, and all of the constellations of Hercules and Corona Borealis. This structure has been given the popular name of the Hercules-Corona Borealis Great Wall, or Her-CrB GW.

We estimate the size of the Her-CrB GW to be about 2000-3000 Mpc across. Few limits on its radial thickness exist, other than because it appears to be confined to the $1.6 \leq z < 2.1$ redshift range. This large size makes the structure inconsistent with current inflationary Universal models because it is larger than the roughly 100 Mpc limit thought to signify the End of Greatness at which large-scale structure ceases.

However, the Her-CrB GW is not the first optical/infrared structure found to exceed the 100 Mpc size limit. Several large filamentary structures have been identified using optical and infrared redshifts of galaxies; these include the 200 Mpc-sized CfA2 Great Wall (Geller & Huchra 1989) and the 400 Mpc-sized Sloan Great Wall (Gott et al. 2005). In the ensuing years, other structures have been identified using quasars; the largest of these is the Huge Large Quasar Group (Huge-LQG) Clowes et al. (2013), which has a length of more than 1400 Mpc. Most recently, Szapudi et al. (2015) found a 440 Mpc diameter supervoid aligned with a cold spot on the cosmic microwave background.

On the other hand, many results support the cosmological principle. Yahata et al. (2005) reported that the galaxy distribution was homogeneous on scales larger than $60 - 70 h^{-1}$ Mpc. Bagla et al. (2008) showed that the fractal dimension makes a rapid transition close to 3 at 40 - 100 Mpc scales. Sarkar et al. (2009) found the galaxy distribution to be homogeneous at length-scales greater than $70 h^{-1}$ Mpc, and Yadav et al. (2010) estimated the homogeneity upper limit scale was close to $260 h^{-1}$ Mpc.

As large as it appears to be, the Her-CrB GW does not necessarily have to violate the basic assumptions of the cosmological principle (the assumptions of a homogeneous and isotropic Universe). Theoretical large-scale structure models indicate that some structures will exceed the End of Greatness on purely statistical grounds (Nadathur 2013), and this may be one such structure (albeit a very large one). Along these lines, this may not be a single structure, but a clustering of smaller adjacent and/or line-of-sight structures; the small number of bursts currently found in the cluster limits our ability to angularly resolve it. However, this becomes a semantic issue at some point, since a cluster of smaller structures is still a larger structure.

Acknowledgements. This research was supported by OTKA grant NN111016 and by NASA EPSCoR grant NNX13AD28A. We thank the anonymous referee for comments that greatly improved this paper.

References

Bagla, J. S., Yadav, J., & Seshadri, T. R. 2008, MNRAS, 390, 829

- Balázs, L. G., Mészáros, A., & Horváth, I. 1998, *A&A*, 339, 1
- Balázs, L. G., Mészáros, A., Horváth, I., & Vavrek, R. 1999, *A&AS*, 138, 417
- Baumgartner, W. H., Tueller, J., Markwardt, C. B., et al. 2013, *ApJS*, 207, 19
- Briggs, M. S., Paciesas, W. S., Pendleton, G. N., et al. 1996, *ApJ*, 459, 40
- Cline, D. B., Matthey, C., & Otwinowski, S. 1999, *ApJ*, 527, 827
- Clowes, R. G., Harris, K. A., Raghunathan, S., et al. 2013, *MNRAS*, 429, 2910
- Geller, M. J. & Huchra, J. P. 1989, *Science*, 246, 897
- Gott, III, J. R., Jurić, M., Schlegel, D., et al. 2005, *ApJ*, 624, 463
- Horváth, I., Hakkila, J., & Bagoly, Z. 2013, 7th Huntsville Gamma-Ray Burst Symposium, GRB 2013: paper 33 in eConf Proceedings C1304143
- Horváth, I., Hakkila, J., & Bagoly, Z. 2014, *A&A*, 561, L12
- Litvin, V. F., Matveev, S. A., Mamedov, S. V., & Orlov, V. V. 2001, *Astronomy Letters*, 27, 416
- Magliocchetti, M., Ghirlanda, G., & Celotti, A. 2003, *MNRAS*, 343, 255
- Mészáros, A., Bagoly, Z., Horváth, I., Balázs, L. G., & Vavrek, R. 2000, *ApJ*, 539, 98
- Nadathur, S. 2013, *MNRAS*, 434, 398
- Sarkar, P., Yadav, J., Pandey, B., & Bharadwaj, S. 2009, *MNRAS*, 399, L128
- Schlafly, E. F. & Finkbeiner, D. P. 2011, *ApJ*, 737, 103
- Szapudi, I., Kovács, A., Granett, B. R., et al. 2015, *MNRAS*, 450, 288
- Vavrek, R., Balázs, L. G., Mészáros, A., Horváth, I., & Bagoly, Z. 2008, *MNRAS*, 391, 1741
- Yadav, J. K., Bagla, J. S., & Khandai, N. 2010, *MNRAS*, 405, 2009
- Yahata, K., Suto, Y., Kayo, I., et al. 2005, *PASJ*, 57, 529

List of Objects

6. Appendix

Table 2. The ID, duration, coordinates, and redshift of the 361 GRBs as were published at <http://lyra.berkeley.edu/grbox/grbox.php>.

GRB	T90	RA	Dec	z
090429B	5.5	210.66688	32.17064	9.4
090423	10.3	148.88871	18.14939	8.2
120923A	27.2	303.79492	6.22119	8
080913A	8	65.72775	-25.1295	6.7
060116	35	84.69283	-5.43698	6.6
050904	225	13.71221	14.08661	6.295
120521C	26.7	214.28668	42.14478	6
130606A	276.6	249.39662	29.7964	5.91
060927	22.6	329.55008	5.36358	5.467
050814	65	264.18912	46.33933	5.3
071025	109	355.07116	31.77858	5.2
050502B	7	142.54192	16.99625	5.2
060522	69	322.93667	2.88621	5.11
111008A	63.46	60.451	-32.70928	4.9898
060510B	276	239.12167	78.57	4.9
100302A	17.9	195.51542	74.59014	4.813
100513A	84	169.61129	3.62789	4.8
100219A	18.8	154.20217	-12.56656	4.6667
090205	8.8	220.91104	-27.85297	4.6497
120401A	100	58.08258	-17.63569	4.5
000131	50	93.37917	-51.94444	4.5
060223A	11	55.2065	-17.1301	4.41
080916C	66	119.84717	-56.63833	4.35
080129	48	105.28404	-7.84628	4.349
050505	60	141.76392	30.2735	4.27
120712A	14.7	169.58846	-20.03383	4.1745
090516A	210	138.26092	-11.85428	4.109
060206	11	202.93092	35.051	4.059
100518A	30	304.78917	-24.55456	4
050730	155	212.07137	-3.77158	3.9693
120909A	112	275.73633	-59.44836	3.93
060210	255	57.73904	27.02622	3.9122
090519	64	142.27917	0.18031	3.85
081029	270	346.77233	-68.15548	3.8479
081228	3	39.46225	30.85292	3.8
120802A	50	44.84313	13.76867	3.796
050502A	20	202.44304	42.67425	3.793
060605	15	322.1555	-6.05869	3.773
130408A	28	134.40542	-32.36081	3.758
60906	43.6	40.7535	39.36164	3.6856
070721B	340	33.13729	-2.19461	3.6298
090323	150	190.70954	17.05322	3.57
060115	142	54.03467	17.34531	3.5328
0980329	15	105.65842	38.84556	3.5
051028	12	27.06254	47.75256	3.5
061110B	128	323.91833	6.87614	3.4344
0971214	50	179.10979	65.21167	3.43
060707	68	357.07917	-17.90472	3.424
121201A	85	13.46738	-42.94289	3.385
090313	78	198.40088	8.09717	3.375
030323	25.05	166.53917	-21.77033	3.372
080810	106	356.79375	0.31944	3.3604

Table 3.

GRB	T90	RA	Dec	z
110818A	103	317.33769	-63.98119	3.36
061222B	40	105.3525	-25.86	3.355
050908	20	20.46146	-12.95478	3.3467
050319	15	154.199	43.54858	3.2425
060526	13.8	232.8265	0.2847	3.2213
060926	8	263.93192	13.0385	3.2086
080516	5.8	120.6415	-26.15933	3.2
020124	45.91	143.21171	-11.51961	3.198
100316A	7	251.97875	71.82708	3.155
111123A	290	154.84642	-20.64472	3.1516
120922A	173	234.7485	-20.18172	3.1
091109A	48	309.25754	-44.15822	3.076
060607A	100	329.71	-22.49631	3.0749
081028A	260	121.89471	2.30808	3.038
080607	79	194.94671	15.91969	3.0368
121217A	778	153.71003	-62.35098	3
090404	84	239.23967	35.51597	3
090715B	266	251.33967	44.83897	3
070411	101	107.33304	1.06461	2.954
120118B	23.26	124.871	-7.18475	2.943
051008	16	202.87313	42.09814	2.9
060306	61	41.09546	-2.14833	2.9
050401	38	247.87008	2.18745	2.8983
111107A	26.6	129.47775	-66.52008	2.893
120404A	38.7	235.0095	12.88503	2.876
110731A	38.8	280.50412	-28.53717	2.83
050603	6	39.98705	-25.18183	2.821
120327A	62.9	246.86442	-29.415	2.813
130427B	27	314.89842	-22.54636	2.78
081222	24	22.73996	-34.09486	2.77
091029	39.2	60.17742	-55.95556	2.752
090809	5.4	328.67996	-0.08384	2.737
060714	115	227.86021	-6.56619	2.7108
090726	67	248.67935	72.88467	2.71
121229A	100	190.10121	-50.5943	2.707
050406	3	34.46792	-50.1875	2.7
071031	180	6.40529	-58.0595	2.6918
080603B	60	176.53192	68.06111	2.6892
120811C	26.8	199.68254	62.30075	2.671
030429	9.19	183.28125	-20.91381	2.6564
080210	45	251.26671	13.82669	2.6419
090529	100	212.469	24.45894	2.625
070103	19	352.5575	26.87622	2.6208
050215B	10	174.449	40.79581	2.62
050820A	26	337.40879	19.56031	2.6147
090426	1.2	189.07529	32.986	2.609
130514A	204	296.28292	-7.97622	2.6
060923A	51.7	254.61733	12.36081	2.6
080721	16.2	224.48273	-11.72348	2.5914
081118A	67	82.59242	-43.30147	2.58
050915A	25	81.68668	-28.01646	2.5273
081121	14	89.27579	-60.60286	2.512
050819	36	358.75675	24.86083	2.5043
030115A	17.94	169.63596	15.04997	2.5
070529	109	283.74246	20.65944	2.4996
130518A	48	355.66781	47.46493	2.49
120716A	230	313.05042	9.59825	2.48

Table 4.

GRB	T90	RA	Dec	z
080515	21	3.1625	32.57806	2.47
100424A	104	209.44762	1.53858	2.465
070802	16.4	36.89867	-55.52747	2.4541
090812	66.7	353.20229	-10.60472	2.452
071021	225	340.64296	23.71847	2.452
080413A	46	287.299	-27.67781	2.433
051001	190	350.95304	-31.52314	2.4296
080310	365	220.0575	-0.17558	2.4274
080905B	128	301.74121	-62.56306	2.3739
120815A	9.7	273.95758	-52.13114	2.358
070110	85	0.91363	-52.97414	2.3521
051109A	25	330.3138	40.82314	2.346
110128A	30.7	193.89629	28.06544	2.339
070129	460	37.00392	11.68444	2.3384
021004	52.4	6.72783	18.92822	2.323
060111A	13	276.205	37.60392	2.32
070506	4.3	347.21829	10.72231	2.309
121024A	69	70.47208	-12.29069	2.298
130505A	88	137.061	17.48478	2.27
081221	34	15.79258	-24.54769	2.26
060124	710	77.10833	69.74089	2.23
110205A	257	164.62967	67.52533	2.22
080804	34	328.6675	-53.18461	2.2045
121128A	7.52	300.60004	54.29978	2.2
050922C	5	317.38785	-8.75839	2.1995
070810A	11	189.96342	10.75119	2.17
071020	4.2	119.66575	32.86111	2.1462
011211	270	168.82492	-21.94894	2.14
060604	10	337.22921	-10.9155	2.1357
090926A		353.40015	-66.32407	2.1062
100728B	12.1	44.05617	0.28106	2.106
060512	8.6	195.77421	41.1909	2.1
081203A	294	233.03158	63.52081	2.1
130610A	46.4	224.42033	28.20711	2.092
061222A	72	358.26425	46.53294	2.088
080207	340	207.51221	7.50186	2.0858
000926	25	256.04046	51.78611	2.066
070611	12	1.99171	-29.75556	2.0394
000301C	10	245.0775	29.44333	2.0335
060108	14.4	147.00825	31.91906	2.03
130612A	4	259.79408	16.71997	2.006
121011A	75.6	260.21342	41.11039	2
080906A	147	228.04438	-80.51756	2
030226	22.09	173.27054	25.89869	1.986
081008	185.5	279.95833	-57.43111	1.967
070419B	236.5	315.70758	-31.26369	1.9588
050315	96	306.47542	-42.60061	1.95
080319C	34	258.98121	55.39183	1.9492
060814	146	221.33871	20.58631	1.9229
060708	9.8	7.80758	-33.759	1.92
020127	7.95	123.75592	36.77608	1.9
060908	19.3	31.8265	0.342	1.8836
131011A	77	32.52658	-4.41119	1.874
110801A	385	89.43721	80.95589	1.858
090902B	21	264.93896	27.32419	1.822
090709A	89	289.92767	60.72758	1.8
120326A	69.6	273.90467	69.25986	1.798
080325	128.4	277.89267	36.52342	1.78

Table 5.

GRB	T90	RA	Dec	z
121027A	62.6	63.59767	-58.82983	1.773
110422	25.9	112.04608	75.10694	1.77
100425A	37	299.1965	-26.43081	1.755
090113	9.1	32.0575	33.42842	1.7493
120119A	253.8	120.02887	-9.08158	1.728
100906A	114.4	28.68379	55.63044	1.727
050802	13	219.27371	27.78672	1.7102
091020	34.6	175.72992	50.97831	1.71
070521	37.9	242.66092	30.25622	1.7
080928	280	95.07015	-55.19971	1.6919
080603A	180	279.40858	62.74425	1.688
080605	20	262.12529	4.01556	1.6403
0990510	100	204.53183	-80.49689	1.619
110503A	10	132.77608	52.20753	1.613
0990123	63.3	231.37642	44.76642	1.61
090418A	56	269.31321	33.40592	1.608
071003	150	301.8505	10.94772	1.6044
070714A	2	42.93046	30.24306	1.58
100728A	198.5	88.75838	-15.25567	1.567
040912	150	359.179	-0.92217	1.563
051111	47	348.13783	18.37461	1.55
070125	60	117.82403	31.15114	1.5471
090102		128.24392	33.11419	1.547
080520	2.8	280.19338	-54.99197	1.5457
060719	55	18.432	-48.38092	1.532
030328	92.59	182.70167	-9.34758	1.522
080330	61	169.26873	30.6232	1.5119
080805	78	314.22267	-62.44439	1.5042
060502A	33	240.927	66.60069	1.5026
070306	210	148.09713	10.48202	1.49594
060418	52	236.4275	-3.63889	1.49
120724A	72.8	245.18062	3.50772	1.48
010222		223.05229	43.01839	1.478
110213A	48	42.96429	49.27314	1.46
090407	310	68.97975	-12.67922	1.4485
050318	32	49.71312	-46.39547	1.4436
100814A	174.5	22.47338	-17.99544	1.44
050822	102	51.11342	-46.03333	1.434
080604	82	236.96542	20.55781	1.4171
100901A	439	27.26425	22.75856	1.408
120711A	44	94.6785	-70.99911	1.405
080602	74	19.17571	-9.23219	1.4
100615A	39	177.20542	-19.48117	1.398
111229A	25.4	76.28692	-84.71086	1.3805
050801	20	204.14583	-21.92806	1.38
090927	2.2	343.97254	-70.98036	1.37
100414A	26.4	192.11233	8.69303	1.368
110808A	48	57.26783	-44.19453	1.348
071117	6.6	335.04342	-63.44319	1.331
061121	81	147.22742	-13.1952	1.3145
0990506	150	178.70892	-26.67644	1.307
130511A	5.43	196.64567	18.71	1.3033
130420A	123.5	196.10654	59.42408	1.297
050126	26	278.11321	42.37044	1.29
100724A	1.4	194.54333	-11.1025	1.288
061007	75	46.33167	-50.50069	1.2622
020813A	88.98	296.67446	-19.60134	1.2545
090926B	81	46.30808	-39.00617	1.24

Table 6.

GRB	T90	RA	Dec	z
130907A	115.1	215.892	45.60742	1.238
050408	34	180.57212	10.85261	1.2356
080707	27.1	32.61833	33.10953	1.2322
130418A	300	149.03717	13.66744	1.218
100316B	3.8	163.48812	-45.47267	1.18
060319	12	176.38704	60.01086	1.172
070208	48	197.88586	61.9651	1.165
070518	5.5	254.19875	55.29508	1.16
061126	191	86.60198	64.21068	1.159
130701A	4.38	357.22954	36.10039	1.155
071122	68.7	276.60525	47.07514	1.14
060801	0.5	213.00554	16.98183	1.131
000418	30	186.33042	20.10322	1.11854
0981226	260	352.40417	22.93161	1.11
080413B	8	326.1445	-19.98111	1.1014
0980613	50	154.49092	71.45708	1.0964
091024	1200	339.24875	56.88983	1.092
110213B		41.75588	1.14619	1.083
091208B	14.9	29.39204	16.88967	1.0633
051006	26	110.80633	9.5068	1.059
000911	500	34.64317	7.74103	1.0585
110726A	5.2	286.71692	56.07128	1.036
080411	56	37.97996	-71.30203	1.0301
121211A	182	195.53329	30.1485	1.023
0991216	50	77.38041	11.28535	1.02
021211	2.8	122.24951	6.72719	1.006
110918A	22	32.53912	-27.10544	0.982
071010A	6	288.06093	-32.40199	0.98
081109	190	330.7905	-54.71097	0.9787
091018	4.4	32.18588	-57.54828	0.971
120907A	16.9	74.75	-9.315	0.97
070419A	116	182.74517	39.92533	0.97
0980703	40	359.77779	8.5853	0.967
120722A	42.4	230.4966	13.2513	0.9586
0970828	160	272.10629	59.30236	0.958
071010B	35.7	150.53858	45.73064	0.947
071028B		354.16167	-31.62047	0.94
080319B	50	217.92075	36.30244	0.9382
060912A	5	5.284	20.97161	0.937
051016B	4	132.11583	13.65575	0.9364
070714B	64	57.8425	28.29761	0.923
090510	0.3	333.55267	-26.58411	0.903
070429B	0.5	328.01587	-38.82833	0.9023
091003	21.1	251.51953	36.62521	0.8969
040924	1.2	31.594	16.11344	0.859
101225A	1088	0.19792	44.60067	0.847
080710	120	8.27354	19.50147	0.8454
000210	20	29.81496	-40.65917	0.8452
0990705	45	77.47708	-72.13139	0.842
070318	63	48.48679	-42.94619	0.84
0970508	35	103.45604	79.27208	0.835
050824	25	12.23421	22.60922	0.8278
061217	0.3	160.41383	-21.12281	0.827
071112C	15	39.21221	28.37131	0.8227
110715A	13	237.68371	-46.23515	0.82
070508	21	312.80029	-78.38528	0.82
051022	200	359.01708	19.60669	0.809
100816A	2.9	351.73983	26.57858	0.804

Table 7.

GRB	T90	RA	Dec	z
120729A	71.5	13.07429	49.93975	0.8
060602A	60	149.56938	0.30408	0.787
060202	203.7	35.84587	38.38422	0.785
030528	53.85	256.00129	-22.61944	0.782
080430	16.2	165.31129	51.68569	0.767
061110A	41	336.29146	-2.25886	0.7578
090328	80	90.66529	-41.88161	0.736
050813	0.6	241.98737	11.24919	0.72
101219A	0.6	74.58537	-2.53972	0.718
131004A	1.54	296.11283	-2.95839	0.717
041006		13.70929	1.23469	0.716
111228A	101.2	150.06671	18.29772	0.716
051227	8	125.24212	31.92553	0.714
0991208	60	248.473	46.45583	0.7055
060904B	192	58.2105	-0.72525	0.7029
090814A	80	239.60979	25.63122	0.696
0970228	3.6	75.44421	11.7815	0.695
020405	40	209.513	-31.37275	0.695
080916A	60	336.27579	-57.023	0.6887
111209A	1400	14.34492	-46.80117	0.677
050416A	2.4	188.47747	21.0573	0.6528
100418A	7	256.36287	11.46175	0.6235
110106B	24.8	134.15528	47.00291	0.618
070612A	370	121.37337	37.27089	0.617
050525A	10	278.13571	26.33958	0.606
130215A	65.7	43.50292	13.39539	0.597
050223	23	271.38538	-62.47252	0.5915
060123	900	179.69933	45.51394	0.56
101219B	34	12.23063	-34.56653	0.5519
051221A	1.4	328.70261	16.89088	0.5465
090424	52	189.52129	16.83753	0.544
060729	116	95.38246	-62.37022	0.5428
100621A	63.6	315.3045	-51.10625	0.542
090618	113.2	293.9955	78.35686	0.54
081007A	10	339.96	-40.14689	0.5295
091127	7.1	36.58288	-18.95236	0.49
051117B	8	85.18075	-19.27422	0.481
130831A	32.5	358.62458	29.42967	0.4791
111211A	15	153.09042	11.20833	0.478
070724A	0.4	27.80863	-18.59426	0.457
010921	21.77	343.99958	40.93139	0.45
061006	130	111.03192	-79.19864	0.4377
0990712	30	337.97096	-73.40786	0.43
020819	20	351.83112	6.26554	0.41
061210	85	144.52196	15.62147	0.4095
120714B	159	355.40875	-46.18389	0.3984
071227	1.8	58.13025	-55.98431	0.394
011121		173.62346	-76.02819	0.362
130603B	0.18	172.20063	17.07167	0.356
110328A		251.20805	57.58325	0.354
060428B	58	235.35679	62.02508	0.35
130925A	0	41.179	-26.1531	0.347

Table 8.

GRB	T90	RA	Dec	z
061021	46	145.15058	-21.95122	0.3463
090417B	260	209.69412	47.01806	0.345
130427A	162.8	173.13683	27.69894	0.34
050826	35	87.75658	-2.64328	0.296
060502B	90	278.93971	52.63136	0.287
120422A	5.35	136.90992	14.01875	0.283
050724	3	246.18487	-27.54097	0.258
020903	32.15	342.17642	-20.76925	0.251
050509B	0.13	189.05858	28.98533	0.2249
070809	1.3	203.76896	-22.14189	0.2187
081211B	102	168.26404	53.82992	0.216
040701	60	312.06708	-40.18579	0.2146
030329A	22.76	161.20817	21.52151	0.1687
050709	220	345.36233	-38.97764	0.16
130702A	59	217.31158	15.774	0.145
000607	0.15	38.49475	17.14764	0.1405
060614	102	320.88367	-53.02672	0.1257
061201	0.8	332.13371	-74.57974	0.111
031203	30	120.6265	-39.85003	0.105
060505	4	331.76433	-27.81442	0.089
051109B	15	345.45983	38.67964	0.08
100316D	240	107.62642	-56.25464	0.059
060218	2100	50.41535	16.86717	0.0331
111005A	26	223.28242	-19.73672	0.01326
0980425	30	293.76379	-52.84575	0.0085
080109	500	137.37771	33.13897	0.006494